



HAL
open science

MALS discovery of a rare HI 21 cm absorber at $z \sim 1.35$: Origin of the absorbing gas in powerful active galactic nuclei

P P Deka, N. Gupta, H W Chen, S D Johnson, P. Noterdaeme, F. Combes, E. Boettcher, S A Balashev, K L Emig, G I G Józsa, et al.

► To cite this version:

P P Deka, N. Gupta, H W Chen, S D Johnson, P. Noterdaeme, et al.. MALS discovery of a rare HI 21 cm absorber at $z \sim 1.35$: Origin of the absorbing gas in powerful active galactic nuclei. *Astronomy and Astrophysics - A&A*, 2024, 687, pp.A50. 10.1051/0004-6361/202348464 . hal-04770509

HAL Id: hal-04770509

<https://hal.science/hal-04770509v1>

Submitted on 6 Nov 2024

HAL is a multi-disciplinary open access archive for the deposit and dissemination of scientific research documents, whether they are published or not. The documents may come from teaching and research institutions in France or abroad, or from public or private research centers.

L'archive ouverte pluridisciplinaire **HAL**, est destinée au dépôt et à la diffusion de documents scientifiques de niveau recherche, publiés ou non, émanant des établissements d'enseignement et de recherche français ou étrangers, des laboratoires publics ou privés.

MALS discovery of a rare H I 21 cm absorber at $z \sim 1.35$: Origin of the absorbing gas in powerful active galactic nuclei

P. P. Deka¹, N. Gupta¹, H. W. Chen², S. D. Johnson³, P. Noterdaeme^{4,5}, F. Combes⁶, E. Boettcher^{7,8,9}, S. A. Balashev¹⁰, K. L. Emig^{11,*}, G. I. G. Józsa^{12,13}, H.-R. Klöckner¹², J.-K. Krogager¹⁴, E. Momjian¹⁵, P. Petitjean⁴, G. C. Rudie¹⁶, J. Wagnveld¹², and F. S. Zahedy¹⁶

¹ Inter-University Centre for Astronomy and Astrophysics, Post Bag 4, Ganeshkhind, Pune 411 007, India
e-mail: parthad@iucaa.in

² Department of Astronomy & Astrophysics, The University of Chicago, 5640 South Ellis Avenue, Chicago, IL 60637, USA

³ Department of Astronomy, University of Michigan, Ann Arbor, MI 48109, USA

⁴ Institut d'Astrophysique de Paris, UMR 7095, CNRS-SU, 98bis bd Arago, 75014 Paris, France

⁵ Franco-Chilean Laboratory for Astronomy, IRL 3386, CNRS and Departamento de Astronomía, Universidad de Chile, Casilla 36-D Santiago, Chile

⁶ Observatoire de Paris, Collège de France, PSL University, Sorbonne University, CNRS, LERMA, Paris, France

⁷ Department of Astronomy, University of Maryland, College Park, MD 20742, USA

⁸ X-ray Astrophysics Laboratory, NASA/GSFC, Greenbelt, MD 20771, USA

⁹ Center for Research and Exploration in Space Science and Technology, NASA/GSFC, Greenbelt, MD 20771, USA

¹⁰ Ioffe Institute, 26 Politekhnicheskaya st., St. Petersburg, 194021, Russia

¹¹ National Radio Astronomy Observatory, 520 Edgemont Road, Charlottesville, VA 22903, USA

¹² Max-Planck-Institut für Radioastronomie, Auf dem Hügel 69, 53121 Bonn, Germany

¹³ Department of Physics and Electronics, Rhodes University, PO Box 94, Makhanda 6140, South Africa

¹⁴ Université Lyon 1, ENS de Lyon, CNRS, Centre de Recherche Astrophysique de Lyon UMR5574, 69230 Saint-Genis-Laval, France

¹⁵ National Radio Astronomy Observatory, 1003 Lopezville Rd., Socorro, NM 87801, USA

¹⁶ The Observatories of the Carnegie Institution for Science, 813 Santa Barbara Street, Pasadena, CA 91101, USA

Received 2 November 2023 / Accepted 13 February 2024

ABSTRACT

We report a new, rare detection of H I 21 cm absorption associated with a quasar (only six quasars are known at $1 < z < 2$) toward J2339–5523 at $z_{\text{em}} = 1.3531$, discovered through the MeerKAT Absorption Line Survey (MALS). The absorption profile is broad ($\sim 400 \text{ km s}^{-1}$), and the peak is redshifted by $\sim 200 \text{ km s}^{-1}$ from z_{em} . Interestingly, optical/far-UV spectra of the quasar from the Magellan-MIKE/HST-COS spectrographs do not show any absorption features associated with the 21 cm absorption, despite the coincident presence of the optical quasar and the radio core inferred from a flat-spectrum component with a flux density of $\sim 65 \text{ mJy}$ at high frequencies ($> 5 \text{ GHz}$). The simplest explanation would be that no large H I column ($N(\text{H I}) > 10^{17} \text{ cm}^{-2}$) is present toward the radio core and the optical active galactic nucleus. Based on the joint optical and radio analysis of a heterogeneous sample of 16 quasars ($z_{\text{median}} = 0.7$) and 19 radio galaxies ($z_{\text{median}} = 0.4$) with H I 21 cm absorption detection and matched in 1.4 GHz luminosity ($L_{1.4 \text{ GHz}}$), a consistent picture emerges according to which quasars primarily trace the gas in the inner circumnuclear disk and cocoon created by the interaction of the jet with interstellar medium. They (i.e., quasars) exhibit a $L_{1.4 \text{ GHz}} - \Delta V_{\text{null}}$ correlation and a frequent mismatch of the radio and optical spectral lines. The radio galaxies show no such correlation and likely trace the gas from the cocoon and the galaxy-wide interstellar medium outside the photoionization cone. The analysis presented here demonstrates the potential of radio spectroscopic observations to reveal the origin of the absorbing gas associated with active galactic nuclei that may be missed in optical observations.

Key words. galaxies: ISM – quasars: absorption lines

1. Introduction

Observations and simulations both provide strong support for the feedback from active galactic nuclei (AGN) in regulating the star formation efficiency of the host galaxy (e.g., Croton et al. 2006; Fabian 2012). The impact of AGN feedback on the physical state of cold atomic and molecular gas is of particular importance in this context. Cold atomic and molecular gas represent the raw material for star formation and directly affect the evolutionary track of the galaxy (e.g., Veilleux et al. 2020). Absorp-

tion line studies provide a powerful way to study these phases in the AGN environment. At optical wavelengths, the obscuration of the AGN by dust prevents the detection of dense molecular clouds in absorption. Mostly diffuse (presumably warm, $\sim 10^4 \text{ K}$) H I has been detected through proximate damped Lyman- α absorption (e.g. Ellison et al. 2010), but progress is made to reach colder ($\sim 100 \text{ K}$) and denser phases using H₂ observations (Noterdaeme et al. 2019). At radio wavelengths, H I 21 cm absorption lines in turn provide a dust-unbiased way to probe the cold atomic gas toward the population of radio-loud AGNs.

To date, more than 500 AGN have been searched for H I 21 cm absorption at $0 < z < 5$ (see Morganti & Oosterloo 2018,

* Jansky Fellow of the National Radio Astronomy Observatory.

for a review). Most of the HI 21 cm absorption detections are associated with compact steep spectrum (CSS) and gigahertz-peaked spectrum (GPS) radio sources (sizes < 15 kpc) at low redshifts ($z < 0.3$). The typical HI column densities for an assumed spin temperature of 100 K in the case of detections are 10^{20-21} cm $^{-2}$. The high 21 cm absorption detection rate ($\sim 30\%$) for these detections is thought to be a direct consequence of the fact that these radio sources are young (age $< 10^5$ yr) and still embedded in the interstellar medium (ISM) of gas-rich host galaxy (e.g., Vermeulen et al. 2003; Gupta et al. 2006). This scenario is also supported by the observational signatures of gas outflows that occur at subkiloparsec scales, which result from radio jet-ISM interactions that are detected through an excess of blueshifted absorption lines (e.g., Morganti et al. 2005a,b; Mahony et al. 2013; Geréb et al. 2015; Morganti & Oosterloo 2018). Furthermore, a bulk of 21 cm absorption detections are associated with type II AGNs (i.e., here radio galaxies) that are seen edge-on. This led to the conclusion that a significant portion of the absorbing gas, especially gas represented by strong narrow absorption components, originates in the obscuring torus or galaxy-wide ISM outside the photoionization cone (Pihlström et al. 2003; Gupta et al. 2006; Gupta & Saikia 2006).

Quantifying the evolution with redshift in the properties of cold gas associated with AGN ought to be an obvious goal of HI 21 cm absorption line studies. However, despite great efforts over the past three decades, only a handful of absorption systems are known at $z > 1$: six systems at $1 < z < 2$, and four systems at $2 < z < 3.5$ (e.g., Aditya & Kanekar 2018b; Gupta et al. 2021b; Curran & Whiting 2012). Specifically, most targets at $z > 2$ are powerful quasars ($\log L_{1.4\text{GHz}}(\text{WHz}^{-1}) \gtrsim 27.0$). They show an extremely low HI 21 cm absorption detection rate ($1.6^{+3.8}_{-1.4}\%$), which agrees with the observed rate ($2\text{--}5\%$) of proximate ($\Delta v < 3000$ km s $^{-1}$ from z_{em}) damped Ly α absorbers ($N(\text{HI}) > 10^{20.3}$ cm $^{-2}$; Ellison et al. 2002). Overall, no firm conclusions can be drawn about the redshift evolution because of the small number of high- z detections, the different selection methods that were applied to low- and high- z samples, and the luminosity bias affecting uniformly selected samples (see Aditya & Kanekar 2018a,b; Grasha et al. 2019).

Here, we report the first associated HI 21 cm absorption detection discovered by the ongoing MeerKAT Absorption Line Survey (MALS; Gupta et al. 2017). The corresponding AGN at $z = 1.3531$ is a bona fide quasar (Véron-Cetty & Véron 2001) and an extremely powerful radio source with 1.4 GHz luminosity, $L_{1.4\text{GHz}} = 10^{27.2}$ WHz $^{-1}$. The combination of compact radio emission (< 5.2 kpc; Boettcher et al. 2022) and the steep spectral index ($\alpha \sim -0.8$) – modeled using a power law, $S_\nu \propto \nu^\alpha$ – imply that the radio AGN may be classified as a CSS source (O’Dea & Saikia 2021). Interestingly, no signatures of neutral gas at the HI 21 cm absorption redshift are detected in the optical-ultraviolet spectrum. The joint radio-optical analysis of this case allows us to discuss the origin and distribution of absorbing gas in the vicinity of the radio source.

This paper is structured as follows. In Sect. 2, we present the details of the radio and far-UV (FUV)/optical observations and their data analysis. In Sect. 3, we present the results and explore the possibility that the absorption might occur against the radio-core component. In Sect. 4, we discuss J2339–5523 in the context of other quasars and radio galaxies in the literature with reported HI 21 cm detections, and we draw general conclusions about the origin of the absorbing gas. The results are summarized in Sect. 5.

Throughout this paper, we use a flat Λ cosmology with $\Omega_{\text{m}} = 0.315$, $\Omega_{\Lambda} = 0.685$, and $H_0 = 67.4$ km s $^{-1}$ Mpc $^{-1}$ (Planck Collaboration VI 2020). At $z = 1.3531$, $1'' = 8.642$ kpc.

2. Observations and data analysis

2.1. Radio observations

J2339–5523 was observed with the MeerKAT-64 array using the 32K mode of the SKA Reconfigurable Application Board (SKARAB) correlator, on 2020 June 14 and 22 (L -band; 856–1712 MHz), and on 2021 January 07 (UHF-band; 544–1088 MHz). The details of the L -band datasets providing a total on-source time of 112 min are presented in Boettcher et al. (2022). For the UHF observations, the SKARAB correlator was configured to split the 544 MHz bandwidth centered at 815.9917 MHz into 32 768 frequency channels. We also observed J0408-6545 for the flux density scale, delay, and band-pass calibrations, and we observed J2329–4730 for the complex gain calibration. The data were acquired in all four polarization products XX, XY, YX, and YY. The correlator dump time was 8 seconds. The total integration time on J2339–5523 was 120 min.

The data were flagged, calibrated, and imaged using the automated radio telescope imaging pipeline (ARTIP) described in Gupta et al. (2021a). The details of the Stokes- I continuum and spectral line imaging steps specific to the L - and UHF-band datasets were presented in Gupta et al. (2021a) and Combes et al. (2021), respectively. The spectral line processing in ARTIP proceeds by splitting the band into 15 spectral windows, labeled SPW0 to SPW14, and it generates continuum images and spectral line image cubes for each of them. For the continuum and spectral line imaging, we used Briggs weighting with a robust factor of 0, as implemented in the Common Astronomy Software Applications (CASA; McMullin et al. 2007). In Fig. 1, we show Stokes- I continuum images of the lowest- and highest-frequency spectral windows from the UHF and L bands, respectively. The restoring beams for these images at 580.1 MHz and 1642.3 MHz are $23''.2 \times 15''.0$ (position angle = -46.2°) and $7''.2 \times 5''.5$ (position angle = $+11.8^\circ$), respectively. The corresponding flux densities at these frequencies, that is, 363.7 ± 0.6 mJy at 580.1 MHz and 166.0 ± 0.1 mJy at 1642.3 MHz, lead to a spectral index of $\alpha_{580}^{1642} = -0.753 \pm 0.002$. The rms noise values close to the central bright source are $300 \mu\text{Jy beam}^{-1}$ and $50 \mu\text{Jy beam}^{-1}$, respectively. The radio emission is unresolved in these images, and using the 1642.3 MHz image, we estimate a deconvolved size $< 0''.6$ (see also Boettcher et al. 2022). At $z = 1.35$, the 21 cm line frequency falls in the SPW1 of the UHF-band, covering 594.983–633.233 MHz and centered at 614.1 MHz (restoring beam = $21''.6 \times 14''.3$; position angle = -45.7°). Using a single-component Gaussian fit to the radio emission, we estimate the total continuum and peak flux density of the source to be 343.0 ± 0.7 mJy and 336.4 ± 0.5 mJy beam $^{-1}$, respectively.

Since the radio emission associated with J2339–5523 is unresolved in the MeerKAT images, we extracted spectra at the pixel ($3''$) corresponding to the peak intensity. As shown in Fig. 2, we clearly detect HI 21 cm absorption associated with J2339–5523. At the detected frequency, based on the spectra of other radio sources observed in MALS, there is no known RFI, and the absorption is consistently detected in the XX and YY spectra. The absorption profile can be well modeled (reduced $\chi^2 = 1.04$) with two Gaussians. The details of the fit and the values of the best-fit parameters are given in Table 1. The velocity width between the nulls of the absorption profile (ΔV_{null}) is ~ 400 km s $^{-1}$. The channel width and rms noise in the vicinity of the redshifted HI 21 cm line frequency in the unsmoothed spectrum are 8.3 km s $^{-1}$ and 1.1 mJy beam $^{-1}$ channel $^{-1}$. The spectrum presented in Fig. 2 has been normalized using the peak flux density of the continuum emission.

2.2. Far-ultraviolet and optical absorption spectra

Medium-resolution, high signal-to-noise ratio (S/N) FUV spectra of J2339–5523 were obtained under the Cosmic Ultraviolet Baryon Survey (CUBS) program (PID = 15163; PI: Chen) using the Cosmic Origins Spectrograph (COS; Green et al. 2012) on board the *Hubble Space Telescope* (HST). The COS FUV spectra offer a contiguous spectral coverage of $\lambda = 1100\text{--}1800 \text{ \AA}$, with a full width at half maximum (FWHM) of the instrumental function of $\sim 20 \text{ km s}^{-1}$. Optical échelle spectra of J2339–5523 were obtained using the Magellan Inamori Kyocera Echelle (MIKE; Bernstein et al. 2003) spectrograph on the *Magellan Clay Telescope*, which cover a wavelength range of $\lambda = 3330\text{--}9300 \text{ \AA}$ with an $FWHM \sim 8 \text{ km s}^{-1}$. The details regarding the observations and data reduction of MIKE spectra were presented in Chen et al. (2020). All spectra were continuum-normalized using a low-order polynomial fit to spectral regions free of strong absorption features.

The final combined COS spectrum of the quasar has a median S/N per resolution element of $\langle S/N \rangle_{\text{resol}} = 22$ over the FUV spectral window. The final combined optical échelle spectrum has an $\langle S/N \rangle_{\text{resol}} = 15$ at $\lambda \sim 3500 \text{ \AA}$. The joint COS FUV and MIKE optical échelle spectra of this quasar provide an extended spectral coverage to constrain the abundances of neutral gas and associated metal ions along the line of sight. Specifically, at $z = 1.3531$, sensitive constraints can be obtained for He I, C II, C IV, O III, Al II, Al III, Mg II, Fe II, and Ca II. However, the hydrogen Lyman series lines are redshifted outside of the COS FUV window. No direct UV absorption constraints are available for H I.

3. Results

3.1. H I 21 cm absorption line gas

The neutral hydrogen column density $N(\text{H I})$, spin temperature T_s , and covering factor of the radio emission by the absorbing gas (f_c) are related to the integrated optical depth ($\int \tau dv$), through

$$N(\text{H I}) = 1.823 \times 10^{18} \frac{T_s}{f_c} \int \tau(v) dv \text{ cm}^{-2}. \quad (1)$$

The absorption profile presented in Fig. 2 corresponds to $\int \tau dv = 3.7 \pm 0.2 \text{ km s}^{-1}$. Assuming $T_s = 100 \text{ K}$ and $f_c = 1$, the total column density is $(6.7 \pm 0.4) \times 10^{20} (T_s/100)(1/f_c) \text{ cm}^{-2}$. The spin temperature is directly controlled by collisions, absorption of 21 cm continuum radiation, and pumping by Ly α photons (Field 1958). In the neighborhood of AGN, the radiative effects may dominate and $T_s \gg 100 \text{ K}$ (Maloney et al. 1996). In order to derive $N(\text{H I})$, we also need constraints on the fraction of radio continuum emission covered by the absorbing gas in addition to T_s , that is, f_c which may be lower than 1. The assumptions of $T_s = 100 \text{ K}$ and $f_c = 1$ therefore provide a lower limit to the true $N(\text{H I})$.

3.2. Comparison with the optical/UV spectral line

Despite the absorption detected in H I 21 cm, no absorption transitions in the UV are seen in available FUV and optical spectra of the quasar. As described in Sect. 2.2, the available HST COS and Magellan MIKE spectra provide spectral coverage for He I, C II, C IV, O III, Al II, Al III, Mg II, Fe II, and Ca II at the redshift of the 21 cm absorber. In Fig. 3, we show FUV/optical spectra at the

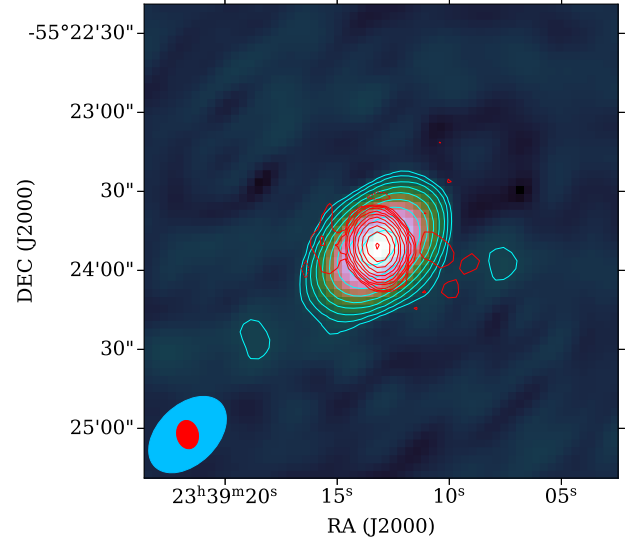


Fig. 1. Portion of the larger ($6k \times 6k$ pixels) MeerKAT Stokes- I continuum images centered on the quasar J2339–5523. The background is the UHF-band image at 580.1 MHz (SPW0). The contour levels are $n \times (-1, 1, 2, 4, 8, 16, \dots)$, where $n = 1.0 \text{ mJy beam}^{-1}$ (cyan) and $0.15 \text{ mJy beam}^{-1}$ (red) for the UHF- and L -band images at 580.1 MHz (SPW0) and 1642.3 MHz (SPW14), respectively. The restoring beams are shown as ellipses in the bottom left corner of the image. The shapes of the cyan and red contours simply follow the corresponding restoring beams, as expected for the unresolved emission (see text for details).

Table 1. Multiple Gaussian fits to the H I absorption in J2339–5523.

Id.	z_{abs}	Centre (km s^{-1})	σ (km s^{-1})	τ_p (10^{-3})
Stokes I ; $\chi^2_{\text{red}} \sim 1.04$				
G_0	1.3546 ± 0.0002	195 ± 35	34 ± 11	10.4 ± 3.2
G_1	1.3539 ± 0.0004	105 ± 23	98 ± 13	12.8 ± 1.9

locations of some of these lines. Clearly, no absorption features are seen in the vicinity of the 21 cm absorption to within sensitive column density limits. The lack of both low- and intermediate-ionization species indicates that the absence of signals is unlikely due to the ionization state of the gas. Furthermore, the lack of He I, a nonmetal, indicates that the absence of cold-gas signatures cannot be attributed to a possibly low metal content. While the data do not provide coverage for the hydrogen Lyman series lines, the observed 2σ upper limit of He I can be converted into an H I column density limit of $\log N(\text{H I})/\text{cm}^{-2} < 15.2$ (e.g., Qu et al. 2023). In Fig. 3 and Table 2, we present the constraints imposed by C IV, Mg II, and He I. These are the strongest UV transitions available at this redshift.

It is worth mentioning here that in the FUV band ($\lambda_{\text{eff}} \sim 1528 \text{ \AA}$) of the Galaxy Evolution Explorer (GALEX; Bianchi et al. 2017) observations, the quasar is detected with an AB magnitude of 17.91 mag. This detection directly rules out the presence of a DLA, or even a Lyman limit system (LLS), at $z = 1.3531$ along the UV line of sight, regardless of any assumptions about the metallicity or the ionization state. This is because the Lyman limit at $z = 1.3531$ occurs at a much redder wavelength ($\lambda \sim 2146 \text{ \AA}$) than the cutoff of the GALEX FUV filter. If there were such a strong H I absorber toward the sight line, GALEX would not detect the quasar in the FUV images.

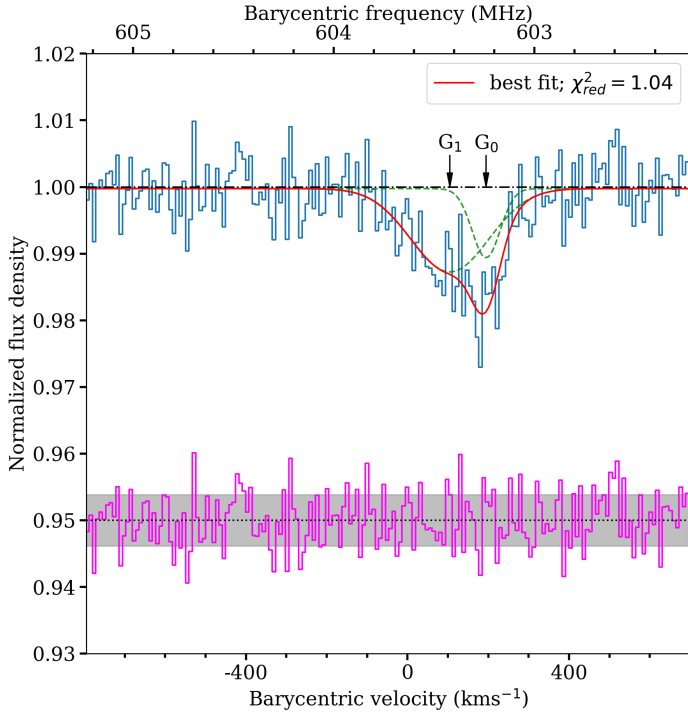


Fig. 2. H I 21 cm absorption associated with J2339–5523. Zero velocity corresponds to $z_{\text{em}} = 1.3531$. Individual Gaussian components (Table 1) and the combined best-fit model are overplotted as dashed (green) and continuous lines (red), respectively. The residuals from the fit (magenta curve) and the 1σ uncertainty on the normalized flux density (shaded region in gray), arbitrarily offset for clarity, are also shown.

3.3. Origin of the absorbing gas

The CSS sources such as J2339–5523 typically exhibit a core-jet or a double-lobed structure reminiscent of large-scale radio sources (O’Dea & Saikia 2021). Since J2339–5523 is a quasar, we anticipate a dominant core component. Nearly simultaneous high-frequency radio observations at 5, 8, and 20 GHz from the AT20G survey carried out using the Australia Telescope Compact Array (ATCA) over 2004–2008 (Murphy et al. 2010) exhibit a flat spectrum component ($\alpha_{\text{ATCA}} = -0.3 \pm 0.2$) with flux densities of 102 ± 5 , 69 ± 4 and 65 ± 3 mJy, respectively. We note that in the W3 (12 μm) and W4 (24 μm) bands of the Wide-field Infrared Survey Explorer (WISE; Wright et al. 2010; Cutri et al. 2014), the quasar has a brightness of 8.475 ± 0.022 mag and 6.033 ± 0.047 mag, respectively. For non-AGN sources, the 33 GHz flux density ($S_{33\text{GHz}}$) in mJy is related to the flux density at 24 μm ($f_{24\mu\text{m}}$) in mJy through $f_{24\mu\text{m}} = 140 \times S_{33\text{GHz}}^{0.94}$ (Murphy et al. 2012). The W3 and W4 band flux densities correspond to rest frame fluxes at $\sim 5 \mu\text{m}$ and $\sim 10 \mu\text{m}$, respectively. Assuming that a simple power law holds in the range (5–24 μm), we derived the rest frame 24 μm flux density to be ~ 235 mJy, corresponding to $S_{33\text{GHz}} \sim 1.73$ mJy. Using this value, we found that the mid-infrared flux density, if due to star formation, only contributes about 2.7% to the optically thin emission detected in AT20G measurements (rest frequency ~ 10 –40 GHz and core flux density ~ 65 mJy). Hereafter, we consider the entire flux density of this quasar as measured in the AT20G survey to be associated with the AGN, that is, the radio core.

The detected H I 21 cm absorption may stem from gas within the circumnuclear disk, it might arise from kinematically disturbed gas affected by AGN or stellar feedback, or it might

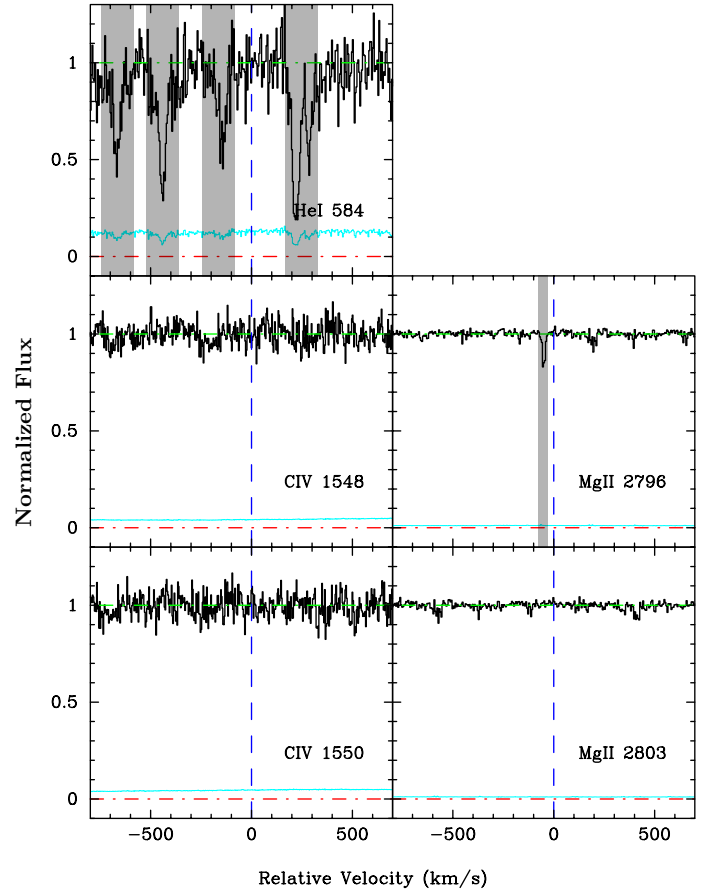


Fig. 3. Constraints on the UV absorption features for a subset of strong transitions commonly seen in quasar absorption-line surveys. Zero velocity corresponds to the quasar emission redshift $z_{\text{em}} = 1.3531$. Contaminating features associated with systems in the foreground at $z < z_{\text{em}}$ are grayed out. At this redshift, H I Lyman series lines are redshifted out of the COS FUV spectral coverage.

Table 2. UV absorption line constraints for G0 and G1 fitted to the 21 cm line.

Species	$\log N_X/(\text{cm}^{-2})$	
	G0	G1
C IV	<12.5	<12.7
Mg II	<11.5	<11.5
He I	<13.6	<13.4

originate in the regularly rotating gas within the galactic disk. Depending on the location, extent, and clumpiness of the gas, it may cover the radio emission only partially. Due to its central location, the detection of absorption toward the radio core or the absence of it can provide crucial constraints on the origin of the absorbing gas (see e.g., Carilli et al. 1998; Gupta et al. 2022). In the case of J2339–5523, the contribution of the radio core to the detected 21 cm absorption primarily depends on its brightness near the 21 cm line frequency and on the actual column density of the gas. For a given column density and covering factor, the strength of the H I 21 cm absorption toward the core can be suppressed in the following two ways: (i) suppression of the background radio continuum due to free-free absorption (FFA) or synchrotron self-absorption (SSA), or (ii) excitation

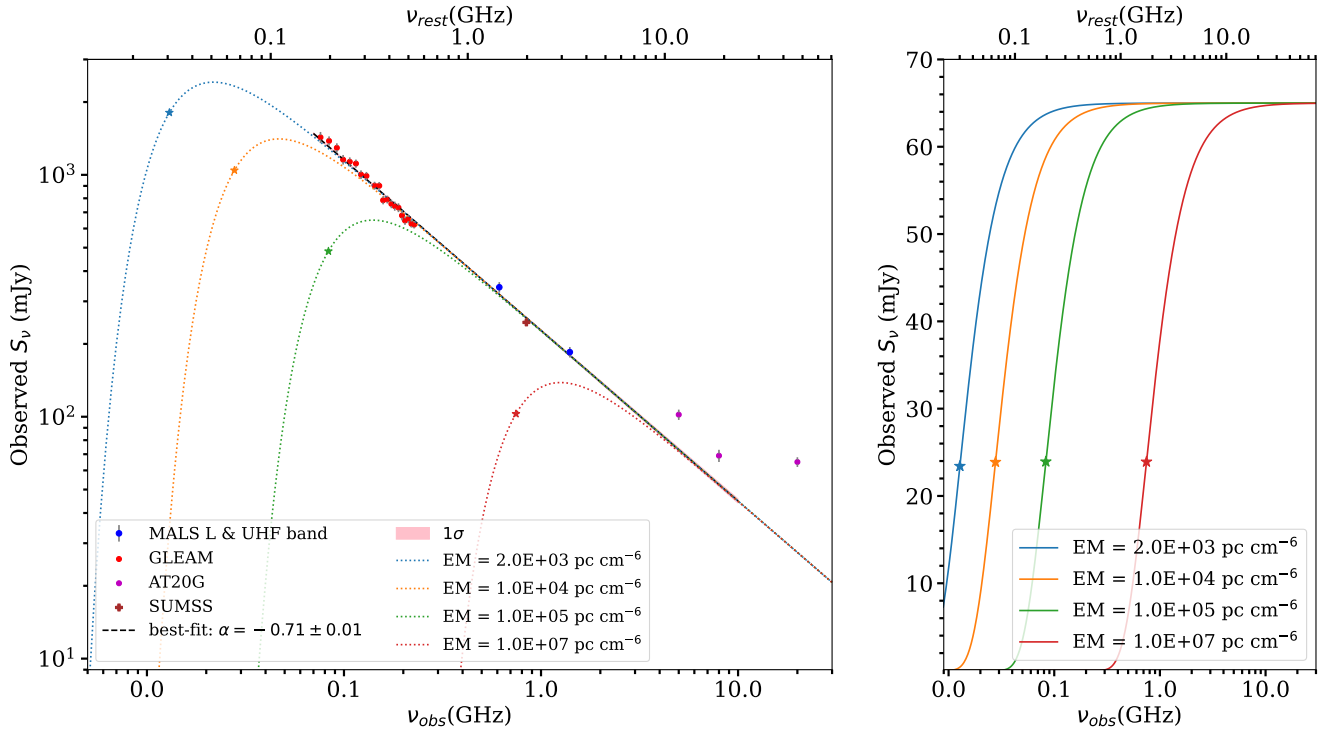


Fig. 4. Spectral energy distribution (SED) of the compact quasar (J2339–5523) and its flat-spectrum core component. Left panel: SED of J2339–5523 obtained by combining measurements from GLEAM (red circles), the MALS *L*- and UHF-bands (blue circles), SUMSS (brown plus), and the AT20G catalog (magenta circles). A power-law ($S_\nu \propto \nu^\alpha$) fit (dashed black line) to the MALS and GLEAM flux densities yields a spectral index, $\alpha = -0.71 \pm 0.01$. The dotted lines represent the SED attenuated by FFA due to a range of emission measures. Right panel: attenuation of the flat-spectrum core component due to FFA for a range of emission measures. In both panels, asterisks represent ν_p (see Sect. 3.3).

mechanisms that increase the spin temperature of the gas, especially due to the proximity to the AGN.

For the modification of radio SED, both FFA and SSA may provide viable solutions. In the latter case, however, the models strongly depend on the flux density and the frequency of the low-frequency turnover, and also on the size of the radio sources (e.g., [Orienti & Dallacasa 2012](#); [Callingham et al. 2015](#); [Shao et al. 2022](#)). Since we do not have observational constraints on either of these, we considered the viability of a simple homogeneous FFA scenario ([Bicknell et al. 1997](#)). To verify this, we assumed that the determination of radio SED is not affected by temporal variability. This is a reasonable assumption considering that a single power-law model can provide a reasonable fit ($\alpha = -0.71 \pm 0.01$) to GLEAM, SUMSS, and MALS *L*- and UHF-band measurements spread over more than 20 years (see the left panel of Fig. 4).

The attenuation, that is, the optical depth, due to FFA is related to the electron temperature (T_e) in Kelvin, to the frequency (ν) in GHz, and to the free electron density (n_e) in cm^{-3} through

$$\tau_\nu = 8.24 \times 10^{-2} \left[\frac{T_e}{\text{K}} \right]^{-1.35} \times \left[\frac{\nu}{\text{GHz}} \right]^{-2.1} \times \left[\frac{\text{EM}}{\text{pc cm}^{-6}} \right], \quad (2)$$

where $\text{EM} = \int n_e^2 dl$ is the emission measure, and l is the distance through the screen in pc ([Mezger & Henderson 1967](#)). In the left panel of Fig. 4, we also show the observed SED attenuated by the FFA optical depth, $\tau_\nu = (\nu/\nu_p)^{-2.1}$, where ν_p is the frequency at which the FFA optical depth is 1. We assumed $T_e = 10^4$ K. At the lowest-frequency measurements from GLEAM, no signature of flattening in the radio SED is observed. This implies that any

external screen covering the radio source has an emission measure of $< 2 \times 10^3 \text{ pc cm}^{-6}$ (see the dotted blue curve in the left panel of Fig. 4).

However, it is possible that the radio core is embedded in a denser environment. In the right panel of Fig. 4, we show the attenuation of the radio core flux density due to FFA. Clearly, an external ionized screen with an emission measure ($\text{EM} \sim 10^7 \text{ pc cm}^{-6}$) is required to attenuate the continuum flux density of the flat-spectrum core component at the redshifted H I 21 cm line frequency to a few mJy such that it does not produce detectable 21 cm absorption. The unresolved emission from the source does not allow us to further investigate the scenario in which the core is attenuated by FFA. Hence, while the suppression due to FFA cannot be completely ruled out, the non-detection ($\log N(\text{H I})/\text{cm}^{-2} < 13.8$) of associated UV absorption signatures in the optical spectrum (Fig. 3) points toward the simplest scenario in which no high H I column ($N(\text{H I}) > 10^{17} \text{ cm}^{-2}$) is present toward the radio core and optical AGN, regardless of whether the core is attenuated by FFA. The optical/UV observations also rule out the possibility of a high- T_s H I gas in front of the radio core. In the absence of any direct constraints on the morphology of the radio source, hereafter, we assume it to possess the canonical structure comprising a radio core with lobes on its either side, which is viewed close to the jet axis.

4. Properties of absorbing gas: Is J2339–5523 unique?

The properties of H I 21 cm absorption associated with radio sources are known to be related to the orientation and size of

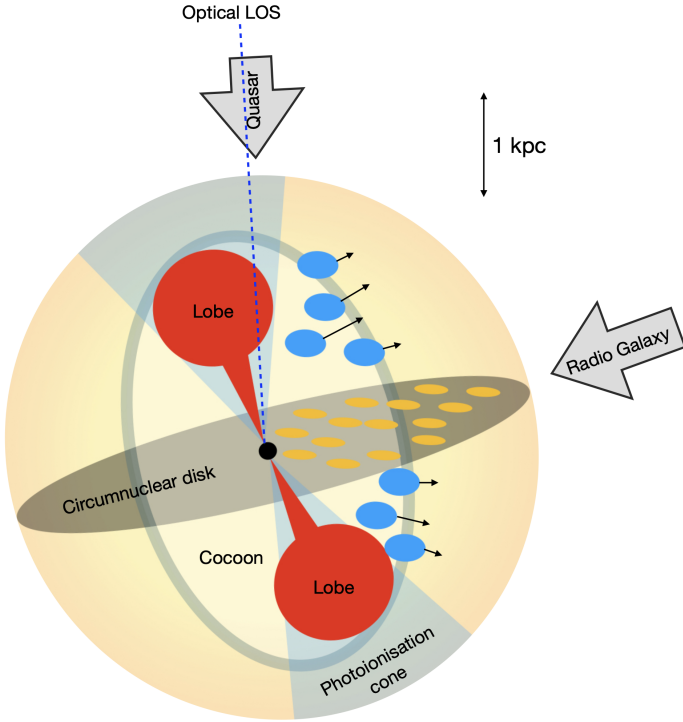


Fig. 5. Cartoon depicting quasar and radio galaxy views of an AGN. The HI clouds in yellow are located in the circumnuclear disk, and the clouds in blue are offset from the disk plane. The optical line of sight is indicated by the dashed blue line, sampling only little of the HI clouds. The sight lines to the quasars primarily pass through photoionization cone and sample cold gas closer to the jet axis and inner circumnuclear disk. The receding lobe would sample both positive and negative velocities corresponding to blue clouds. The galaxy view, with a weak core, primarily samples cold gas from blue clouds (negative velocities) in front of the lobes and the galaxy-wide ISM outside the photoionization cone.

the source. Among compact radio sources (<15 kpc), the detection rates are found to be significantly lower for quasars than radio galaxies (Gupta & Saikia 2006). This is consistent with the unification scheme, implying that the lines of sight to the radio components for quasars more frequently pass through the ionization cone, which is in general devoid of cold gas (see Fig. 5). Trace molecular gas has been detected through these channels as well, however (Noterdaeme et al. 2021). The jet axis is not always perfectly aligned with respect to the circumnuclear disk (Ruffa et al. 2020), and a jet-ISM interaction may also push the gas over a wider range of angles, forming a cocoon, thereby increasing its covering factor for absorption (Wagner et al. 2012; Mukherjee et al. 2016). Additionally, this jet-ISM interaction can also cause the development of the strong large-scale outflows, which can entrain a large amount of the gas and facilitate the formation of the cold gas by condensation of the medium in the envelope of the shocked gas (e.g., Villar-Martín et al. 1999; Morganti 2017). These factors along with the intrinsic misalignment in the radio morphology may produce HI 21 cm absorption in some of these cases (e.g., Gupta et al. 2022).

At optical wavelengths, the detection of HI clouds can be tricky because of leaking Ly- α emission (e.g. Finley et al. 2013; Fathivavvavari et al. 2018), but the presence of cold gas in the quasar environment can be revealed by H₂ absorption toward the central engine (Noterdaeme et al. 2019). In these cases, large molecular reservoirs likely in the host galaxy are also frequently seen from CO emission (e.g., Dasyra & Combes 2012;

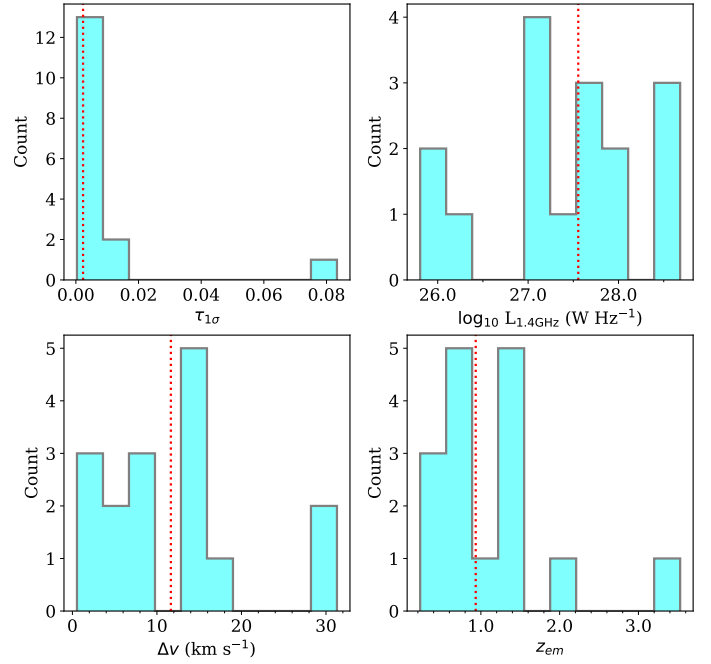


Fig. 6. Distribution of $\tau_{1\sigma}$ (top left), radio luminosity at 1.4 GHz ($L_{1.4\text{GHz}}$ in W Hz^{-1} ; top right), spectral resolution ($\Delta\nu$ in km s^{-1} ; bottom left), and redshift (z_{em} ; bottom right) for the sample of 16 quasars (including J2339–5523) with associated HI 21 cm detections. The vertical dotted lines indicate the median values of each parameter on the x-axis.

Noterdaeme et al. 2023). At redshifted 21 cm line frequencies, the prominent jets and lobes along with the radio core provide multiple sight lines to more efficiently sample the distribution and kinematics of gas in the circumnuclear disk and host galaxy ISM (see Fig. 5).

In the literature, HI 21 cm absorption detections associated with 15 quasars have been reported (see Table A.1). They form a very heterogeneous sample that spans a wide range in redshift ($z_{\text{em}} = 0.2\text{--}3.5$) and 1.4 GHz spectral luminosity ($L_{1.4\text{GHz}} = 10^{26\text{--}29} \text{ W Hz}^{-1}$). The quasars were observed with varied spectral resolution in terms of $\Delta\nu$ ($0.54\text{--}31.3 \text{ km s}^{-1}$) and optical depth sensitivity ($\tau_{1\sigma}$). These basic properties are listed in Table A.1, and their distributions are shown in Fig. 6. We smoothed all the spectra to a common velocity resolution of $\sim 30 \text{ km s}^{-1}$ and measured the following two quantities as proxies for gas kinematics from the absorption profiles: (i) ΔV_{null} , that is, width between the nulls of the absorption profile (in km s^{-1}) indicating the velocity spread of the absorbing gas; and, (ii) $A_p = |V_{\text{null,B}}| - |V_{\text{null,R}}|$ to quantify the blue- or redward asymmetry in the line profile. To measure ΔV_{null} , we fit the smoothed absorption profile using multiple Gaussians and determined nulls as velocities when the fitted profile fell below 1σ optical depth sensitivity. In Table A.1, we provide the blueward ($V_{\text{null,B}}$) and redward ($V_{\text{null,R}}$) null velocities with respect to the 21 cm absorption peak. From these, ΔV_{null} can be obtained using $\Delta V_{\text{null}} = |V_{\text{null,B}} - V_{\text{null,R}}|$. For J2339–5523, $\Delta V_{\text{null}} = 397 \text{ km s}^{-1}$ is typical of the quasar sample. However, the profile is slightly redshifted with an absorption peak at $\sim 200 \text{ km s}^{-1}$ (Fig. 2). The absorption component G_1 is consistent with the systemic velocity and may represent clouds in the circumnuclear disk. The redshifted component G_0 may then correspond to inflowing gas. This simplistic interpretation is compromised by the simultaneous possibility of multiple origins of the gas, however (Combes & Gupta 2024).

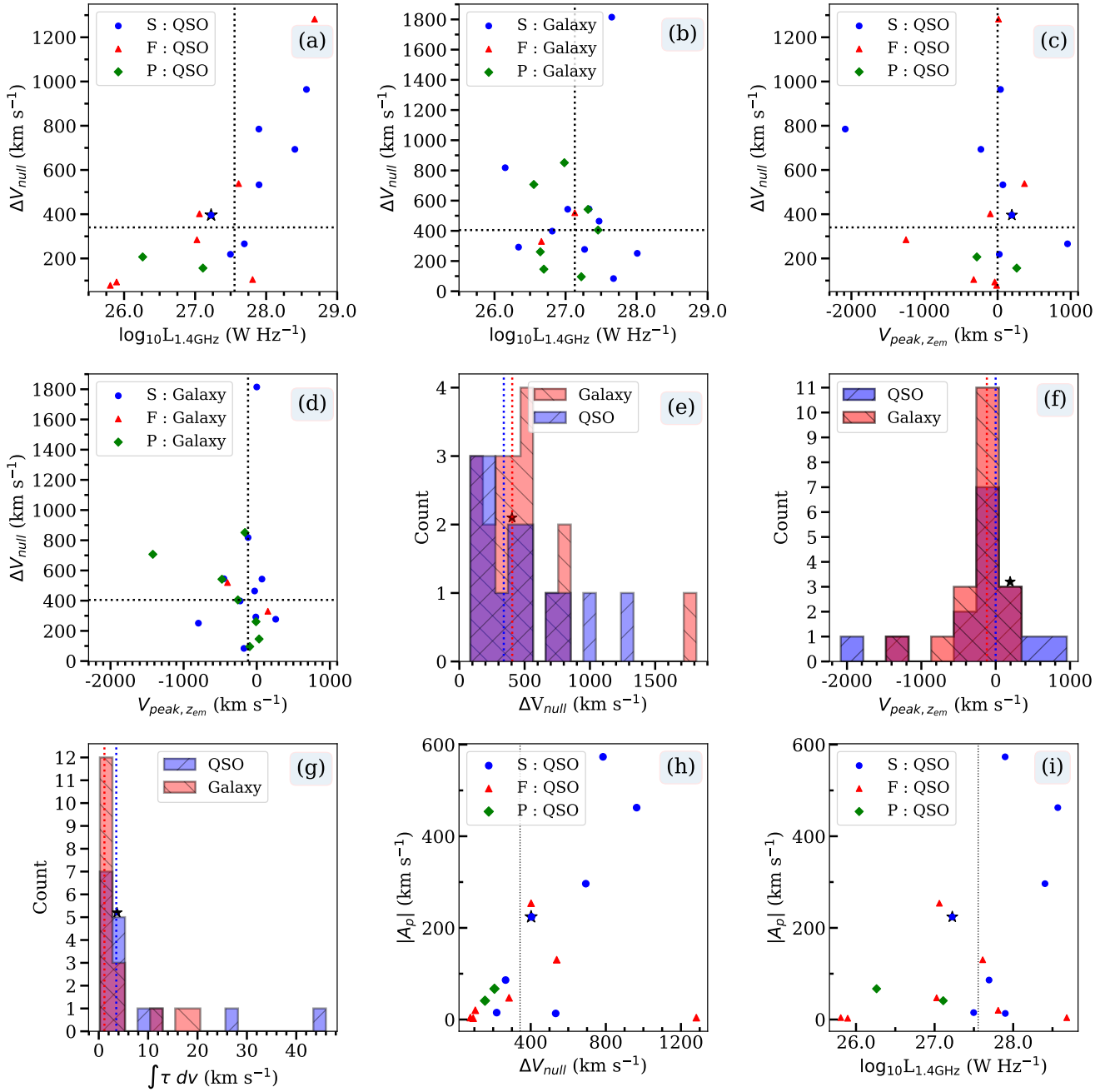


Fig. 7. Distributions of various observables associated with the HI 21 cm absorption line and radio continuum associated with quasars (16) and radio galaxies (19). Different symbols and colors are used for systems with different radio SEDs: steep spectrum (S, filled blue circles), peaked spectrum (P, filled green diamonds) and flat spectrum (F, filled red triangles). In all the panels, the dotted lines mark the median. The location of J2339–5523, a steep-spectrum source, is shown using a five-point star.

We investigated the origin of the absorbing gas by comparing the HI absorption properties of the quasar sample with a sample of 19 radio-galaxies from the literature (Vermeulen et al. 2003; Aditya 2019), matched in 1.4 GHz luminosity with the quasar sample and have an associated HI 21 cm absorption detection. The details are provided in Table B.1. For the quasar sample, we find a significant correlation between $L_{1.4\text{GHz}}$ and ΔV_{null} (Kendall’s tau coefficient, $r = 0.65$ and $p\text{-value} = 2 \times 10^{-4}$). The corresponding scatter plot is shown in Fig. 7a. Interestingly, ΔV_{null} for radio galaxies exhibits no correlation ($r = -0.08$; $p\text{-value} = 0.68$; Fig. 7b). However, the extent of the absorption lines is similar to that of the quasar sample (Figs. 7c–f). The

galaxies show marginally larger ΔV_{null} (KS test $p\text{-value} = 0.70$) and blueshifts (KS test $p\text{-value} = 0.37$) measured with respect to optical redshifts. We do not find any significant correlations between $|A_p|$ and $L_{1.4\text{GHz}}$ either for quasars and galaxies. However, between $|A_p|$ and ΔV_{null} a moderate correlation for quasars and a relatively stronger correlation for galaxies is observed. The Kendall tau-coefficients and $p\text{-values}$ for quasars and galaxies are 0.48 and 0.008, and 0.60 and 0.0001, respectively. This suggests that broader lines associated with powerful AGN ($L_{1.4\text{GHz}} > 10^{26} \text{ W Hz}^{-1}$) may also be more asymmetric, as seen among relatively less powerful AGN ($L_{1.4\text{GHz}} = 10^{24-26} \text{ W Hz}^{-1}$; Maccagni et al. 2017).

The quasars and radio galaxies with different radio SEDs, that is, steep spectrum (S; $\alpha \leq -0.5$), peaked spectrum (P; turnover at GHz frequencies), and flat spectrum (F; $\alpha > -0.5$), are also distinguished in Fig. 7. The spectral classifications provide important information on both the size and nature of the background radio emission. Radio sources with higher turnover frequencies are more compact, and vice versa, flatter spectra indicate a dominant core component, while emission from older population of electrons (e.g., lobes) gives rise to steeper spectra. Generally, core-dominated and peaked-spectrum sources have smaller projected largest linear sizes (LLS) estimated from milliarcsecond-scale images (see Tables A.1 and B.1). However, we note that LLS have been estimated using high-frequency (>2.3 GHz) milliarcsecond-scale images and present only a very approximate picture of radio emission close to the HI 21 cm line frequencies. Nevertheless, we find no significant correlation between LLS and ΔV_{null} for the quasar sample ($r = 0.27$; p -value = 0.17), indicating that the observed $L_{1.4\text{GHz}}$ and ΔV_{null} relation is not affected by other observables such as the LLS (see Fig. 9 of Gupta et al. 2012).

The luminosity ($L_{1.4\text{GHz}}$) and redshift are strongly correlated in the quasar sample. A varying optical depth sensitivity in a given sample, either due to the selection of brighter AGNs or poor spectral rms, may also affect the measurements of ΔV_{null} and A_p . A Kendall tau test for the quasars indicates a weak anticorrelation, with a statistical significance lower than 2σ ($\text{tau} = -0.35$, p -value = 0.07). This suggests that sensitivity issues due to Malmquist bias affect our results very little, as illustrated in Fig. 8. We note that 14 out of the 16 systems ($\sim 88\%$) in the quasar sample exhibit optical depth sensitivities within 1σ of the median sensitivity (Fig. 6). We investigated the potential biases due to optical depth sensitivity by dividing the quasar sample into two equal groups at median $\tau_{1\sigma,30}$. We then upscalded the rms noise in the spectra with better sensitivities to match the common median $\tau_{1\sigma,30}$ of the lower-sensitivity subset. This rendered absorption profiles of 5 systems unsuitable for the analysis. The remaining 11 systems still exhibit a correlation between ΔV_{null} and $L_{1.4\text{GHz}}$ ($\text{tau} = 0.56$, p -value = 0.01). However, the weaker correlation between ΔV_{null} and $|A_p|$ seen in Fig. 7h disappeared. We were unable to perform a similar detailed investigation for the sample of radio galaxies due to the unavailability of adequate information in the literature. However, since these are generally bright radio sources, we do not expect any additional biases, except due to any intrinsic redshift evolution among quasars ($z_{\text{median}} = 0.7$) and radio galaxies ($z_{\text{median}} = 0.4$).

Overall, the correlation of $L_{1.4\text{GHz}}$ and ΔV_{null} among powerful quasars but not radio galaxies suggests that the orientation of the AGN may play an important role in the observed gas properties. As illustrated in Fig. 5, in the radio-galaxy view, the sight lines toward the radio lobes would be effective in tracing the kinematically disturbed gas within the cocoon created by the jet-ISM interaction and galaxy-wide ISM outside the photoionization cone. In the quasar view, the jet axis is closely aligned with the line of sight. Therefore, a significant portion of the absorbing clouds, particularly at extreme velocities, may (scenario 1) originate from the inner circumnuclear disk and experience the strong gravitational field of the central black hole, or (scenario 2) may be perturbed by energy output associated with radio jets. Since powerful AGN are associated with massive red galaxies (e.g., Goulding et al. 2014), the role of starbursts in gas perturbations may be ignored. The conclusion is also supported by the mid-infrared colors of AGN considered here (see Wright et al. 2010). In line with scenario 1, the integrated optical

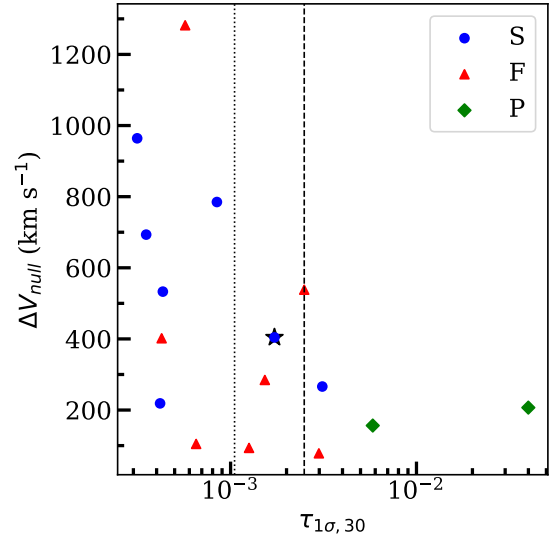


Fig. 8. Velocity width between the nulls of the absorption profiles, ΔV_{null} (in km s^{-1}) as a function of $\tau_{1\sigma,30}$ for all the 16 quasars listed in Table A.1. The markers and dotted vertical lines are same as in Fig. 7. The dashed vertical line marks the median $\tau_{1\sigma,30}$ of higher $\tau_{1\sigma,30}$ bin.

depths toward quasars that probe the inner regions of the galaxy with a higher filling factor of cold gas are also marginally higher (Fig. 7g; KS test p -value = 0.05). Figure 5 illustrates that in the quasar view (scenario 2), the sight line toward the receding lobe may trace both inflowing and outflowing clouds (<1 kpc for the sample), exhibiting positive and negative velocities, respectively, thereby resulting in symmetric line profiles. This may explain the less asymmetric absorption lines observed in the case of quasars and the broader or more blueshifted absorption profiles observed among radio galaxies. Scenario 1 assumes that more powerful quasars at higher redshifts in the sample are associated with more massive black holes. While this cannot be ruled out (Labita et al. 2009), a larger complete sample observed with uniform sensitivity is required to draw conclusions.

Interestingly, despite the incompleteness of the sample and the nonuniform quality and wavelength coverage of the radio spectra, the case of J2339–5523 does not appear unique. In all of the above, it is interesting to note that J2339–5523 exhibits typical properties among quasars with HI 21 cm absorption (see the five-pointed star in Fig. 7).

Finally, we examined the generality of the discrepancy between radio and optical sight lines in the case of J2339–5523 using the samples in Tables A.1 and B.1. Optical spectra are available for five quasars (see Table A.2). In only one case are absorption lines of Mg II and Mg I, indicators of high- $N(\text{HI})$ gas, detected. Among the remaining four cases, no absorption is detected. Even in the case of J080133.56+141443.0, although strong Mg II doublets as well as Mg I absorption lines are detected in the SDSS DR6 spectrum (Adelman-McCarthy et al. 2008), the radio core is self-absorbed at the frequency of the HI 21 cm absorption (Ishwara-Chandra et al. 2003). Hence, toward J0801+1414, the cold gas seen in the 21 cm absorption is not against the radio core and does not correspond to the gas that produces the metal absorption in the optical spectrum.

Optical spectra adequate to search for absorption lines are available for 7 out of 19 radio galaxies (see Table A.2) In all the cases, the signatures of cold gas through the absorption lines of Ca II $\lambda\lambda 3934, 3969$ and/or Na I $\lambda\lambda 5891, 5897$ are reliably detected. The peak absorption in 5 out of 6 cases also matches

the HI 21 cm absorption well. The increased occurrence of a concurrent cold-gas detection in both radio and optical observations for radio galaxies suggests that they both trace the same population of clouds in the less clumpy outer regions of the galaxy.

5. Summary

We have reported the detection of HI 21 cm absorption associated with the quasar J2339–5523 at $z = 1.3531$. These detections are rare, and only six quasars are known at $1 < z < 2$. The detected absorption profile is wide, with a velocity width between nulls of $\Delta V_{\text{null}} = 397 \text{ km s}^{-1}$. However, the profile is slightly redshifted, with an absorption peak at $\sim 200 \text{ km s}^{-1}$ (Fig. 2). Assuming $T_s = 100 \text{ K}$ and $f_c = 1$, we derived a lower limit to $N(\text{HI}) \geq 6.7 \times 10^{20} \text{ cm}^{-2}$. Interestingly, the FUV and optical spectra toward this source obtained using HST/COS and MIKE spectrographs, respectively, do not reveal any signature of metal absorption. The simplest explanation would be that no high HI column ($N(\text{HI}) > 10^{17} \text{ cm}^{-2}$) is present toward the radio core and the optical AGN.

Based on the joint optical and radio analysis of a heterogeneous sample of 16 quasars ($z_{\text{median}} = 0.7$) and 19 radio galaxies ($z_{\text{median}} = 0.4$) with HI 21 cm absorption and matched in 1.4 GHz luminosity ($L_{1.4\text{GHz}} > 10^{26} \text{ W Hz}^{-1}$), a consistent picture emerges according to which powerful quasars that exhibit a correlation between $L_{1.4\text{GHz}}$ and ΔV_{null} trace the gas in the inner circumnuclear disk and/or clouds close to the jet axis that is perturbed by the jet-ISM interaction. Consistent with this, the integrated optical depths toward quasars probing the inner regions of the galaxy with a higher filling factor of cold gas are also marginally higher. In contrast, the radio galaxies have absorption lines of similar extent, but exhibit no correlation with the $L_{1.4\text{GHz}}$. These absorbers most likely trace the gas from the extended cocoon that is created by the jet-ISM interaction and the galaxy-wide ISM outside the photoionization cone. The absorption associated with them is also marginally broader, more asymmetric, and blueshifted with respect to the systemic velocity. While these data exhibit the different origins of absorbing gas detected in quasars and radio galaxies, a larger complete sample observed with uniform sensitivity is required for an exact interpretation.

The HI 21 cm absorption detection toward J2339–5523 and the analysis presented here demonstrate the potential of radio spectroscopic observations, even when they are spatially unresolved, to reveal the origin of the absorbing gas through multiple sight lines toward core, jet, and lobes. In the near future, a clearer picture of the origin and structure of the absorbing gas will emerge from the larger samples from the ongoing surveys (Gupta et al. 2017; Allison et al. 2022; Hu et al. 2023). Specifically, in the near future, bright radio sources from MALS will reveal the evolution of cold gas associated with a variety of AGN at $0 < z < 1.5$ (Deka et al. 2024).

Acknowledgements. We thank an anonymous referee for useful comments. The MeerKAT telescope is operated by the South African Radio Astronomy Observatory, which is a facility of the National Research Foundation, an agency of the Department of Science and Innovation. The MeerKAT data were processed using the MALS computing facility at IUCAA (<https://mals.iucaa.in/>). EB acknowledges support by NASA under award number 80GSFC21M0002. The National Radio Astronomy Observatory is a facility of the National Science Foundation operated under cooperative agreement by Associated Universities, Inc. This paper includes data gathered with the 6.5 meter *Magellan* Telescopes located at Las Campanas Observatory, Chile. This paper has utilized data from the Cosmic Origins Spectrograph (COS) onboard HST. This research has made

use of NASA's Astrophysics Data System and the NASA/IPAC Extragalactic Database (NED), which is operated by the Jet Propulsion Laboratory, California Institute of Technology, under contract with the National Aeronautics and Space Administration.

References

- Adelman-McCarthy, J. K., Agüeros, M. A., Allam, S. S., et al. 2008, *ApJS*, **175**, 297
- Aditya, J. N. H. S. 2019, *MNRAS*, **482**, 5597
- Aditya, J. N. H. S., & Kanekar, N. 2018a, *MNRAS*, **473**, 59
- Aditya, J. N. H. S., & Kanekar, N. 2018b, *MNRAS*, **481**, 1578
- Aditya, J. N. H. S., Kanekar, N., Prochaska, J. X., et al. 2017, *MNRAS*, **465**, 5011
- Aditya, J. N. H. S., Jorgenson, R., Joshi, V., et al. 2021, *MNRAS*, **500**, 998
- Albaret, F. D., Allende Prieto, C., Almeida, A., et al. 2017, *ApJS*, **233**, 25
- Allison, J. R., Sadler, E. M., Amaral, A. D., et al. 2022, *PASA*, **39**
- Bernstein, R., Shectman, S. A., Gunnels, S. M., Mochnicki, S., & Athey, A. E. 2003, in *Instrument Design and Performance for Optical/Infrared Ground-based Telescopes*, eds. M. Iye, & A. F. M. Moorwood, *SPIE Conf. Ser.*, **4841**, 1694
- Bianchi, L., Shiao, B., & Thilker, D. 2017, *ApJS*, **230**, 24
- Bicknell, G. V., Dopita, M. A., & O'Dea, C. P. O. 1997, *ApJ*, **485**, 112
- Boettcher, E., Gupta, N., Chen, H.-W., et al. 2022, *ApJ*, **926**, L33
- Britzen, S., Vermeulen, R. C., Taylor, G. B., et al. 2007, *A&A*, **472**, 763
- Callingham, J. R., Gaensler, B. M., Ekers, R. D., et al. 2015, *ApJ*, **809**, 168
- Carilli, C. L., & van Gorkom, J. H. 1992, *ApJ*, **399**, 373
- Carilli, C. L., Wrobel, J. M., & Ulvestad, J. S. 1998, *AJ*, **115**, 928
- Chen, H.-W., Zahedy, F. S., Boettcher, E., et al. 2020, *MNRAS*, **497**, 498
- Combes, F., & Gupta, N. 2024, *A&A*, **683**, A20
- Combes, F., Gupta, N., Muller, S., et al. 2021, *A&A*, **648**, A116
- Croton, D. J., Springel, V., White, S. D. M., et al. 2006, *MNRAS*, **365**, 11
- Curran, S. J., & Whiting, M. T. 2012, *ApJ*, **759**, 117
- Cutri, R. M., Wright, E. L., Conrow, T., et al. 2014, *VizieR Online Data Catalog*: **II/328**
- Dasyra, K. M., & Combes, F. 2012, *A&A*, **541**, L7
- Deka, P. P., Gupta, N., Jagannathan, P., et al. 2024, *ApJS*, **270**, 33
- Deller, A. T., & Middelberg, E. 2014, *AJ*, **147**, 14
- Ellison, S. L., Yan, L., Hook, I. M., et al. 2002, *A&A*, **383**, 91
- Ellison, S. L., Prochaska, J. X., Hennawi, J., et al. 2010, *MNRAS*, **406**, 1435
- Fabian, A. C. 2012, *ARA&A*, **50**, 455
- Fathivavari, H., Petitjean, P., Jamialahmadi, N., et al. 2018, *MNRAS*, **477**, 5625
- Fey, A. L., & Charlot, P. 2000, *ApJS*, **128**, 17
- Field, G. B. 1958, *Proc. IRE*, **46**, 240
- Finley, H., Petitjean, P., Pâris, I., et al. 2013, *A&A*, **558**, A111
- Geréb, K., Maccagni, F. M., Morganti, R., & Oosterloo, T. A. 2015, *A&A*, **575**, A44
- Goulding, A. D., Forman, W. R., Hickox, R. C., et al. 2014, *ApJ*, **783**, 40
- Grasha, K., Darling, J., Bolatto, A., Leroy, A. K., & Stocke, J. T. 2019, *ApJS*, **245**, 3
- Green, J. C., Froning, C. S., Osterman, S., et al. 2012, *ApJ*, **744**, 60
- Gupta, N., & Saikia, D. J. 2006, *MNRAS*, **370**, 738
- Gupta, N., Salter, C. J., Saikia, D. J., Ghosh, T., & Jeyakumar, S. 2006, *MNRAS*, **373**, 972
- Gupta, N., Srianand, R., Petitjean, P., et al. 2012, *A&A*, **544**, A21
- Gupta, N., Srianand, R., Baan, W., et al. 2017, *arXiv e-prints* [arXiv:1708.07371]
- Gupta, N., Jagannathan, P., Srianand, R., et al. 2021a, *ApJ*, **907**, 11
- Gupta, N., Srianand, R., Shukla, G., et al. 2021b, *ApJS*, **255**, 28
- Gupta, N., Srianand, R., Momjian, E., et al. 2022, *ApJ*, **927**, L24
- Helmboldt, J. F., Taylor, G. B., Tremblay, S., et al. 2007, *ApJ*, **658**, 203
- Hu, W., Wang, Y., Li, Y., et al. 2023, *A&A*, **675**, A40
- Ishwara-Chandra, C. H., Dwarakanath, K. S., & Anantharamaiah, K. R. 2003, *J. Astrophys. Astron.*, **24**, 37
- Kanekar, N., & Chengalur, J. N. 2008, *MNRAS*, **384**, L6
- Labita, M., Decarli, R., Treves, A., & Falomo, R. 2009, *MNRAS*, **399**, 2099
- Lawrence, C. R., Zucker, J. R., Readhead, A. C. S., et al. 1996, *ApJS*, **107**, 541
- Liu, X., Cui, L., Luo, W. F., Shi, W. Z., & Song, H. G. 2007, *A&A*, **470**, 97
- Maccagni, F. M., Morganti, R., Oosterloo, T. A., Geréb, K., & Maddox, N. 2017, *A&A*, **604**, A43
- Mahony, E. K., Morganti, R., Emonts, B. H. C., Oosterloo, T. A., & Tadhunter, C. 2013, *MNRAS*, **435**, L58
- Malkin, Z. 2018, *ApJS*, **239**, 20
- Maloney, P. R., Hollenbach, D. J., & Tielens, A. G. G. M. 1996, *ApJ*, **466**, 561
- McMullin, J. P., Waters, B., Schiebel, D., Young, W., & Golap, K. 2007, in *Astronomical Data Analysis Software and Systems XVI*, eds. R. A. Shaw, F. Hill, & D. J. Bell, *ASP Conf. Ser.*, **376**, 127

- Mezger, P. G., & Henderson, A. P. 1967, *ApJ*, **147**, 471
- Morganti, R. 2017, *Front. Astron. Space Sci.*, **4**, 42
- Morganti, R., & Oosterloo, T. 2018, *A&ARv*, **26**, 4
- Morganti, R., Oosterloo, T. A., Tadhunter, C. N., van Moorsel, G., & Emonts, B. 2005a, *A&A*, **439**, 521
- Morganti, R., Tadhunter, C. N., & Oosterloo, T. A. 2005b, *A&A*, **444**, L9
- Mukherjee, D., Bicknell, G. V., Sutherland, R., & Wagner, A. 2016, *MNRAS*, **461**, 967
- Murphy, T., Sadler, E. M., Ekers, R. D., et al. 2010, *MNRAS*, **402**, 2403
- Murphy, E. J., Bremseth, J., Mason, B. S., et al. 2012, *ApJ*, **761**, 97
- Noterdaeme, P., Balashev, S., Krogager, J. K., et al. 2019, *A&A*, **627**, A32
- Noterdaeme, P., Balashev, S., Krogager, J. K., et al. 2021, *A&A*, **646**, A108
- Noterdaeme, P., Balashev, S., Cuellar, R., et al. 2023, *A&A*, **673**, A89
- O’Dea, C. P., & Saikia, D. J. 2021, *A&ARv*, **29**, 3
- Orienti, M., & Dallacasa, D. 2012, *MNRAS*, **424**, 532
- Pihlström, Y. M., Vermeulen, R. C., Taylor, G. B., & Conway, J. E. 1999, *ApJ*, **525**, L13
- Pihlström, Y. M., Conway, J. E., & Vermeulen, R. C. 2003, *A&A*, **404**, 871
- Planck Collaboration VI. 2020, *A&A*, **641**, A6
- Polatidis, A. G., Wilkinson, P. N., Xu, W., et al. 1995, *ApJS*, **98**, 1
- Qu, Z., Chen, H.-W., Rudie, G. C., et al. 2023, *MNRAS*, **524**, 512
- Ruffa, I., Laing, R. A., Prandoni, I., et al. 2020, *MNRAS*, **499**, 5719
- Sanghera, H. S., Saikia, D. J., Luedke, E., et al. 1995, *A&A*, **295**, 629
- Shao, Y., Wagg, J., Wang, R., et al. 2022, *A&A*, **659**, A159
- Sokolovsky, K. V., Kovalev, Y. Y., Pushkarev, A. B., Mimica, P., & Perucho, M. 2011, *A&A*, **535**, A24
- Torrealba, J., Chavushyan, V., Cruz-González, I., et al. 2012, *Rev. Mex. Astron. Astrofis.*, **48**, 9
- Veilleux, S., Maiolino, R., Bolatto, A. D., & Aalto, S. 2020, *A&ARv*, **28**, 2
- Vermeulen, R. C., Pihlström, Y. M., Tschager, W., et al. 2003, *A&A*, **404**, 861
- Véron-Cetty, M. P., & Véron, P. 2001, *A&A*, **374**, 92
- Villar-Martín, M., Tadhunter, C., Morganti, R., Axon, D., & Koekemoer, A. 1999, *MNRAS*, **307**, 24
- Wagner, A. Y., Bicknell, G. V., & Umemura, M. 2012, *ApJ*, **757**, 136
- Wright, E. L., Eisenhardt, P. R. M., Mainzer, A. K., et al. 2010, *AJ*, **140**, 1868

Appendix A: List of quasars from the literature

Here we present the properties of quasars selected from the literature. Table [A.1](#) provides radio continuum and H I 21 cm absorption line details. The details from optical spectra are provided in Table [A.2](#).

Table A.1. Quasars with HI 21 cm absorption from literature.

Source name (1)	z_{em} (opt) (2)	z_{abs} (3)	$V_{null,B}$ (km s ⁻¹) (4)	$V_{null,R}$ (km s ⁻¹) (5)	$S_{1.4GHz}$ (mJy) (6)	α (7)	$\log L_{1.4GHz}^*$ (W Hz ⁻¹) (8)	$S_{21 cm}$ (mJy) (9)	$\int \tau dv$ (km s ⁻¹) (10)	21 cm Ref. (11)	LAS (arcsec) (12)	LLS (kpc) (13)	Ref. (14)
J000557.17+382015.2	0.229	0.229	-45.4	48.2	572.7	-0.03 ± 0.10	25.9	547.3	1.943 ± 0.057	1	0.043	0.162	1, 13
J011137.31+390627.9	0.67	0.668	-69.9	137.0	429.0	2.09 ± 0.05	26.3	180.0	46 ± 7	2	0.005	0.036	19
J050321.20+020304.6	0.5834	0.5848	-98.7	57.7	2245.1	1.07 ± 0.04	27.1	1600.0	3.4 ± 0.4	2	0.011	0.073	19
J061048.87+724853.2	3.52965	3.52983	-643.0	639.0	1041.6	-0.37 ± 0.07	28.7	1790.2	4.69 ± 0.15	3	0.050	0.373	3, 15
J080133.56+141443.0	1.1946	1.1929	-198.4	494.9	2734.6	-1.10 ± 0.11	28.4	5690.0	2.47 ± 0.05	4	4.0	33.0	4
J090933.50+425346.5	0.67	0.67	-259.8	273.5	4234.2	-0.80 ± 0.10	27.9	6218.1	0.68	5,6	9.2	64.5	19
J120321.94+041419.0	1.22429	1.20888	-105.8	679.1	1146.6	-0.65 ± 0.11	27.9	1675.2	2.52 ± 0.12	7	0.075	0.458	7, 16
J124823.89-195918.8	1.275	1.275	-713.3	250.8	5136.1	-0.59 ± 0.04	28.6	8302.2	4.542 ± 0.043	7	0.040	0.230	20
J145844.79+372021.5	0.33324	0.33316	-41.3	37.0	215.1	-0.02 ± 0.03	25.8	148.4	3.834 ± 0.079	1	< 0.01	< 0.0495	1, 14
J150609.53+373051.1	0.674	0.673	-327.8	74.0	937.6	0.05 ± 0.10	27.1	1040.0	27.20 ± 0.04	8,9	0.055	0.387	9, 17
J154015.23-145341.5	2.104	2.1139	-176.1	90.0	203.7	-0.69 ± 0.04	27.7	652.0	11.30 ± 0.07	10	> 0.050	> 0.425	10, 18
J154508.52+475154.6	1.277	1.2797†	-334.5	204.0	685.7	-0.36 ± 0.09	27.6	861.5	9.56 ± 0.36	1	0.060	0.516	11
J181536.79+612711.6	0.601	0.594	-118.6	166.0	849.3	-0.48 ± 0.08	27.0	971.6	2.39	6	0.01	0.068	19
J195542.73+513148.5	1.223	1.2206	-62.5	42.3	1588.1	0.01 ± 0.09	27.8	1254.1	0.716 ± 0.037	12	> 0.050††	> 0.4275††	12
J233913.22-552350.4	1.353	1.355	-86.4	310.8	184.2	-0.71 ± 0.01	27.2	336.0	3.7 ± 0.2	..	< 0.6	< 5.2	..
J225503.88+131333.9	0.543	0.543	-101.8	116.9	2706.8	-0.83 ± 0.11	27.5	3725.5	0.23	6	2.6	16.5	19

References. (1) Aditya & Kanekar (2018b); (2) Carilli et al. (1998); (3) Aditya et al. (2021); (4) Ishwara-Chandra et al. (2003); (5) Pihlsröm et al. (1999); (6) Vermeulen et al. (2003); (7) Aditya & Kanekar (2018a); (8) Carilli & van Gorkom (1992); (9) Kanekar & Chengalur (2008); (10) Gupta et al. (2021b); (11) Malkin (2018); (12) Aditya et al. (2017); (13) Fey & Charlot (2000); (14) Helmboldt et al. (2007); (15) Britzen et al. (2007); (16) Liu et al. (2007); (17) Polatidis et al. (1995); (18) Gupta et al. (2022); (19) Gupta et al. (2006); (20) Sokolovsky et al. (2011). Column 1: Source name (J2000); Column 2: Optical redshift; Column 3: Peak HI 21 cm absorption redshift; Column 4 - 5: Velocity to the bluer and redder side of the peak, respectively, where the optical depth goes below the spectrum sensitivity; Column 6: Flux density at 1.4 GHz; Column 7: Spectral index and its associated uncertainty; Column 8: Radio luminosity at 1.4 GHz; Column 9: Flux density at the redshifted 21 cm line frequency; Column 10: Total velocity integrated optical depth; Column 11: HI 21 cm absorption reference; Column 12: Largest Angular Size in arcsec, and Column 13: Largest Linear Size in kpc; Column 14: Reference for LAS and LLS. † centroid of two Gaussian components of similar amplitudes †† size of the radio-core against which the absorption was observed (see Aditya et al. (2017) for more details) * Derived using 1.4 GHz (NVSS) and 4.85 GHz flux densities from NED. In four cases, the spectral turnover falls between 1.4 GHz and 4.85 GHz, or 4.85 GHz measurement is unavailable or dubious. For these measurements at 1.4 GHz and at a lower frequency were used.

Table A.2. Rest equivalent width (W_r in Å) estimates from optical spectra.

Source name (1)	$z_{em}(\text{opt})$ (2)	Reference (3)	λ_{obs} (Å) (4)	λ_{rest} (Å) (5)	Line (6)	W_r (Å) (7)
Quasars						
J0111+3906 [†]	0.67	1	...	2694–5567	MgII2796, MgI2853	<4.633, <4.633
J0801+1414	1.1946	2	3800–9200	1731–4192	MgII2796, MgI2853	1.865, 1.245
J0909+4253	0.67	2	3800–9200	2275–5509	MgII2796, MgI2853	<0.744, <0.744
J1203+0414	1.22429	2	3800–9200	1708–4136	MgII2796, MgI2853	<0.270, <0.266
J1458+3720	0.33324	2	3800–9200	2852–6900
J1955+5131	1.223	3	5502–9841	2475–4427	MgII2796, MgI2853	<0.316, <0.139
Radio galaxies						
J0834+5534	0.242	2	3800–9200	3059–7407	NaI5891	2.0
J0901+2901	0.194	2	3800–9200	3182–7705	CaII3934, NaI5891	6.8, 1.5
J1013+2448	0.94959	4	3800–9200	1949–4718	CaII3934	1.2
J1247+4900	0.20691	2	3800–9200	3148–7623	CaII3934	6.0
J1400+6210	0.431	2	3800–9200	2655–6429	CaII3934, NaI5891	5.9, 2.7
J1648+2224	0.82266	4	3800–9200	2085–5047	CaII3934	7.0
J2355+4950 [†]	0.2379	1	...	3036–7962	CaII3934, NaI5891	7.8, 3.8

References. (1) [Lawrence et al. \(1996\)](#); (2) [Adelman-McCarthy et al. \(2008\)](#); (3) [Torrealba et al. \(2012\)](#); (4) [Albareti et al. \(2017\)](#). Column 1: Source name (J2000); Column 2: Optical redshift; Column 3: Optical spectrum reference; Column 4: λ range (in Å) covered in the observed frame; Column 5: λ range (in Å) covered in the rest frame; Column 6: Metal lines covered by the wavelength range; Column 7: Rest equivalent width (W_r) estimates or upper limits. [†] the available optical spectrum is in the rest frame.

Appendix B: List of radio galaxies from the literature

Here we present the properties of radio galaxies selected from the literature and matched in $L_{1.4\text{GHz}}$ with the quasar sample.

Table B.1 provides radio continuum and HI 21 cm absorption line details. The details from optical spectra are provided in Table A.2.

Table B.1. Radio galaxy sample with HI 21 cm absorption from literature.

Source name	$z_{em}(\text{opt})$	z_{abs}	$V_{null,B}^{\dagger}$ (km s^{-1})	$V_{null,R}^{\dagger}$ (km s^{-1})	$S_{1.4\text{GHz}}$ (mJy)	$\log L_{1.4\text{GHz}}$ (W Hz^{-1})	$S_{21\text{ cm}}$ (mJy)	$\int \tau dv$ (km s^{-1})	21 cm Ref.	LAS (arcsec)	LLS (kpc)	Ref.
(1)	(2)	(3)	(4)	(5)	(6)	(7)	(8)	(9)	(10)	(11)	(12)	(13)
J0025–2602	0.322	0.322	–349	115	8.753	27.5	8.17	1.33	1	0.65	3.02	3
J0141+1353	0.621	0.620	–225	–141	2.74	27.7	3.78	0.64	1	0.99	6.71	3
J0146–0157	0.959	0.959	–700	1115	882.5	27.65	1803.8	11.46	6	0.04	0.326	9
J0431+2037	0.219	0.219	–54	92	3.756	26.7	4.56	2.00	1	0.29	1.02	3
J0834+5534	0.242	0.240	–672	–152	8.283	27.1	7.22	0.61	1	11.0	41.4	3
J0901+2901	0.194	0.194	–161	131	2.004	26.3	2.006	0.06	1	5.7	18.2	3
J1013+2448	0.950	0.947	–832	–287	541.7	27.33	891.9	1.15	6	0.049	0.396	8
J1048+3538	0.846	0.847	–411	132	309.3	27.03	552.9	4.77	6	0.03	0.236	9
J1206+6413	0.371	0.372	130	407	3.720	27.3	3.34	1.13	1	1.3	6.6	3
J1247+4900	0.207	0.207	–757	61	1.140	26.1	1.226	0.46	2	2.64	5.4	5
J1326+3154	0.370	0.368	–760	–218	4.862	27.3	5.405	0.41	1	0.056	0.285	3
J1357+4354	0.646	0.645	–585	266	0.704	27.0	0.50	19.53	1	0.017	0.117	3
J1400+6210	0.431	0.430	–470	–65	4.308	27.5	5.47	1.10	1	0.065	0.362	3
J1648+2224	0.823	0.824	–68	262	253.0	26.66	252.8	16.06	6	0.0056	0.044	7
J1821+3942	0.798	0.793	–923	–672	3.507	28.0	5.17	0.96	1	0.47	3.53	3
J1944+5448	0.263	0.257	–1782	–1075	1.754	26.6	1.95	2.88	1	0.040	0.161	3
J2052+3635	0.355	0.355	–168	–72	5.144	27.2	4.5	4.24	1	0.060	0.297	3
J2316+0405	0.220	0.219	–405	–803	4.676	26.8	4.97	0.43	1	1.86	6.55	4
J2355+4950	0.238	0.238	–111	150	2.306	26.6	2.25	1.66	1	0.069	0.256	3

References. (1) Vermeulen et al. (2003); (2) Maccagni et al. (2017); (3) Gupta et al. (2006); (4) Grasha et al. (2019); (5) Sanghera et al. (1995); (6) Aditya (2019); (7) Helmboldt et al. (2007); (8) Deller & Middelberg (2014); (9) C-band map from VLBI Calibrator search Column 1: Source name (J2000); Column 2: Optical redshift; Columns 3: Peak HI 21 cm absorption redshift; Column 4 - 5: Velocity to the bluer and redder side of the peak, respectively, where optical depth approaches zero; Column 6: Flux density at 1.4 GHz; Column 7: Radio luminosity at 1.4 GHz; Column 8: Flux density at the redshifted 21 cm line frequency; Column 9: Total velocity integrated optical depth; Column 10: HI 21 cm absorption reference; Column 11: Largest Angular Size in arcsec, and Column 12: Largest Linear Size in kpc; Column 13: Reference for LAS and LLS. [†] measured with respect to $z_{em}(\text{opt})$.